Practical workflow for arbitrary non-circular orbits for CT with clinical robotic C-arms

Yiqun Q. Ma[a], Grace J. Gang[a], Tess Reynolds[b], Tina Ehtiati[c], Junyuan Li[a], Owen Dillon[b], Tom Russ[d], Wenying Wang[a], Clifford Weiss[a], Nicholas Theodore[a], Kelvin Hong[a], Ricky O'Brien[b], Jeffrey Siewerdsen[a], and J. Webster Stayman[a]

[a]Johns Hopkins University, Baltimore, USA
[b]University of Sydney, Sydney, Australia
[c]Siemens Healthineers, Forchheim, Germany
[d]Heidelberg University, Mannheim, Germany

ABSTRACT

Non-circular orbits in cone-beam CT (CBCT) imaging are increasingly being studied for potential benefits in field-of-view, dose reduction, improved image quality, minimal interference in guided procedures, metal artifact reduction, and more. While modern imaging systems such as robotic C-arms are enabling more freedom in potential orbit designs, practical implementation on such clinical systems remains challenging due to obstacles in critical stages of the workflow, including orbit realization, geometric calibration, and reconstruction. In this work, we build upon previous successes in clinical implementation and address key challenges in the geometric calibration stage with a novel calibration method. The resulting workflow eliminates the need for prior patient scans or dedicated calibration phantoms, and can be conducted in clinically relevant processing times.

Keywords: Cone-beam CT, C-arms. non-circular orbits, geometric calibration

1. INTRODUCTION

For decades, CT imaging has largely relied on standard circular and helical source-detector orbits for data acquisition. In recent years, new imaging systems (eg. robotic C-arms) have enabled the exploration of more advanced non-circular orbits for added benefits including increased field-of-view (FOV) size,[1] improved image quality and/or dose reduction,[2] weight-bearing extremity imaging,[3] and metal artifact reduction.[4–7]

Despite the increased interest, non-circular orbits that require more complex motion remain difficult to implement and research on clinical systems. There are several challenges — especially when many new orbits are desired including those that are customized to be patient- and/or task-specific. First, without access to sophisticated control systems, it is difficult to command the system to realize designed orbits. To date, we have relied on largely manual controls to achieve non-circular orbits on robotic C-arms.[4,7,8] Second, the manual element in the data acquisition leads to irreproducible scans. Additionally, the system geometry parameters recorded by the robot are not accurate enough to be used for 3D reconstructions due to system vibrations and gravity-induced strain on mechanical parts. Therefore, each scan requires online geometric calibration before reconstruction. Previously, we used a 3D-2D registration process for geometric calibration, in which we used a prior reconstruction as the registration target and then iteratively register each acquired projection to forward projections from the registration target.[9] However, this method requires a prior reconstruction and relatively long computation time, both of which may not be available in a clinical setting, and thus presents an obstacle to clinical research and translation.

In this work, we outline a workflow for implementing non-circular orbits on clinical systems, focusing on orbits previously demonstrated with inherent metal artifact reduction capabilities. This workflow includes a novel geometric calibration method based on fixed fiducials with arbitrary and *a priori* unknown placement, which overcomes the aforementioned challenges in clinical implementation.

7th International Conference on Image Formation in X-Ray Computed Tomography,
edited by Joseph Webster Stayman, Proc. of SPIE Vol. 12304, 123042H
© 2022 SPIE · 0277-786X · doi: 10.1117/12.2647158

2. METHODS

We introduce a workflow for arbitrary-trajectory CT data acquisition in the following subsections. This includes details of acquisition on an experimental test bench and two different clinical robot C-arms, as well as a new online geometric calibration method and image reconstruction. Many clinical systems are limited in the degree of automatic orbit control. Some currently can only be driven manually while others allow increasing levels of automation. While fully manual techniques allow for research investigations, clinical translation will require additional manufacturer support.

2.1 Orbit Design and Implementation

Previously, we have investigated several types of non-circular orbits that can largely eliminate metal artifacts including *sinusoidal* and *multiple-arc* trajectories.[5–7] In this work we consider simplified versions of two orbit types: *sawtooth orbits* and *double-circle-plus-arc (DCArc) orbits.* (See Figure 1). Both orbits were designed with a fixed isocenter, with LAO/RAO gantry rotation angle and CRAN/CAUD gantry tilt angle being the parameters in non-circular actuation. In the sawtooth orbit, the source oscillated between ±20° in tilt at a constant speed for two full cycles while rotating 360°. The DCArc orbit consisted of two tilted circular scans at ±25° plus an arc, where the gantry did not rotate while tilting from $+29°$ to $-28°$. On the test bench, the orbits were realized by rotating and tilting the object with a 6-degrees-of-freedom hexapod robot (*Experiment A*). On clinical C-arms, the orbits were realized by manually driving using the bedside joystick in fluoroscopy mode (*Experiment B*), manually advancing through pre-programmed navigation points,[7] or using a dedicated control system supplied by the manufacturer (*Experiment C*).

2.2 Geometric Calibration

As mentioned above, calibration of trajectories can require scan-specific estimation of the system geometry. Towards this end, we placed steel ball bearings (BBs) on the surface of the object as fiducials, similar to work by *Li et al.*[10] Their absolute and relative positions with respect to the imaging object and each other were unknown *a priori* but were presumed to remain rigidly aligned with respect to each other and the object during the scan. The locations of BBs in projection images were extracted and used as inputs to a geometric estimation routine. Details of this procedure follow.

2.2.1 BB Extraction

The BB locations were identified in each projection by performing a 2D correlation between the line integral images and a disc-shaped kernel of roughly the same size as the BBs. The highest correlations represent the approximate location of the centroids of the BBs. This location is further refined by computing the centroid of pixel values in a square region-of-interest (ROI) about the initial location estimate. Predicted BB locations based on linear interpolation across adjacent frames were used to identify individual BBs and maintain continuity. For scans where the BBs had very low contrast against background features such as metal and thick bones, the extraction was initialized by manually selecting the approximate centroid locations on the first image.

2.2.2 Geometry Optimization

With accurately calibrated geometry, backprojected rays of the *centroid* of a BB should intersect at an infinitesimal point in space. With an inaccurate geometry, these rays may not intersect. Thus, we can potentially estimate the true geometry by minimizing the mean Euclidean distance from the BB centers to corresponding backprojected rays, or, the *reprojection error* (RPE):

$$\mathbf{RPE}(\mathbf{p}, \Omega_n) = \frac{1}{K}\sum_{k=1}^{K} \mathbf{d}\left[\mathbf{p}_k, \mathbf{L}_k(\Omega_n)\right] \tag{1}$$

where n is the projection index; k is the BB index; Ω_n are parameters of the view-dependent system geometry; $\mathbf{p}$ contains all 3D BB center locations; $\mathbf{L}_k(\Omega_n)$ is the line equation of the ray backprojected from the k-th BB centroid on the n-th projection view using geometry Ω_n; $\mathbf{d}\left[\mathbf{p}, \mathbf{L}\right]$ is the Euclidean distance from point $\mathbf{p}$ to line $\mathbf{L}$.

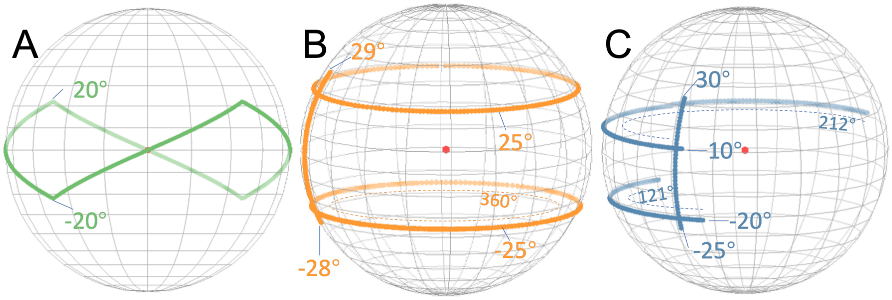

Figure 1. Diagram showing the non-circular orbits invested in this work. Red dot at center of spheres is the isocenter. Colored dots on the sphere are source positions in the orbit. Important CRAN/CAUD tilt angles and arc lengths are marked on each plot. (A) sawtooth orbit. (B) double-circle-plus-arc (DCArc) orbit. (C) multi-arc orbit.

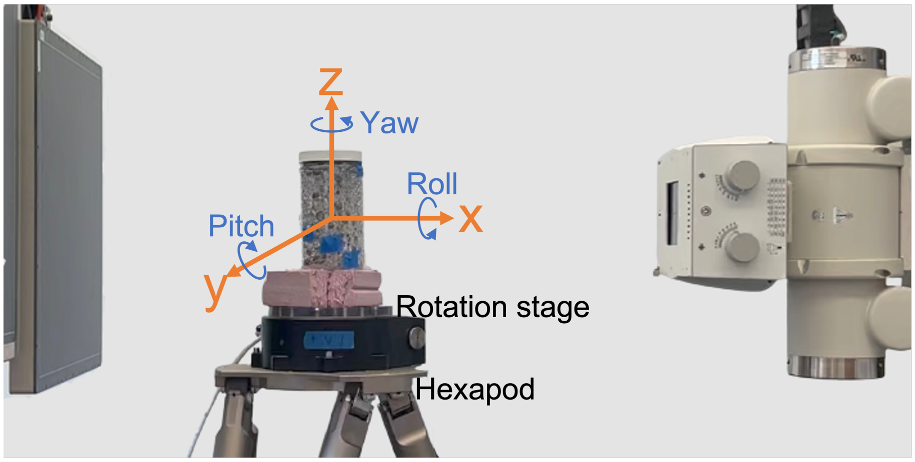

Figure 2. Photo of bench setup and diagram of the 6 DoF motion space of the hexapod stage.

We presume that the BB center locations are unknown (e.g. no prior scan or calibration) and also need to be estimated. We start with an approximate geometry (e.g. based on rough encoder positions or commanded location) as an initial guess. In this case, backprojected lines will likely not intersect at a point but instead a larger region that is generally close to the true BB location in 3D. For each pair of backprojected rays, we calculate the *nearest point* between these rays - the midpoint of the line segment orthogonal to and connecting both rays. We form a point cloud by computing the nearest points between all ray pairs, and the mean location of the point cloud is used as the estimated BB center: $\hat{\mathbf{p}}_k = \overline{\mathbf{P}}_N\left[\mathbf{L}_k(\Omega)\right]$ where $\overline{\mathbf{P}}_N\left[\mathbf{L}(\Omega)\right]$ is the mean of all nearest points formed from N rays backprojected using geometry Ω. We iteratively update $\hat{\mathbf{p}}$ and Ω by minimizing the RPE to jointly estimate BB point cloud centers and the system geometry:

$$\hat{\Omega}_{n,i} = \operatorname*{argmin}_{\Omega} \mathbf{RPE}_n(\hat{\mathbf{p}}_{i-1}, \Omega) \tag{2}$$

where i is the iteration number. Note that the solutions of this objective will have fixed points where the point clouds have shrunk to infinitesimal size. It is possible that such a scenario is not the true geometry; however, such a geometry should provide accurate representations at those points. In this work, the optimization is performed using the MATLAB (MathWorks Inc.) function *fmincon*.

2.3 Reconstruction and Metal Artifact Reduction (MAR)

For image formation for the non-circular scan trajectories, we used a model-based iterative reconstruction algorithm. Specifically, we used a modified Penalized Weighted Least-Squares (PWLS) objective with a quadratic penalty. For all experiments, 50 iterations of a separable paraboloidal surrogates algorithm[11] were applied. A simple MAR algorithm[12] was implemented to eliminate streaks, etc. associated with the BBs or implants. In

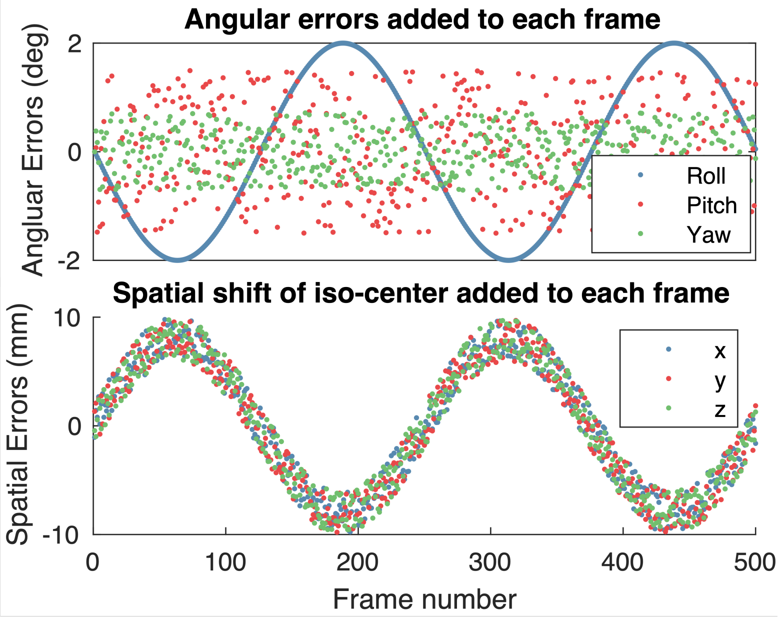

Figure 3. Motion errors added to the sawtooth orbit in Fig. 1 for the test bench experiment. Top plot: angular errors added in roll, pitch, and yaw. Bottom plot: spatial shift of iso-center added in x, y, and z axes.

short, the metal regions in the projection images were segmented and those regions were filled using interpolated data. For implants, the metal volumes were added back into the metal-free reconstruction.

2.4 Experiment A: X-ray Test Bench

To investigate the online registration approach under controlled conditions, we performed a phantom study on a dedicated x-ray testbench.

2.4.1 Phantom Design

The test phantom (Figure 4A) consisted of a 3D-printed cervical spine placed in a plastic cylinder filled with plastic spheres of variable sizes for background clutter. Eight steel BBs of 3.17 mm diameter were affixed to the side of the container. BB placement followed a roughly spiral fashion to reduce the chance of overlapping BBs in projections; however, precise locations were unknown *a priori.*

2.4.2 Bench Experiment Implementation

The test bench includes an X-ray tube (Varex Rad-94), a flat-panel detector (Varex PaxScan 4343CB), a 6 degree-of-freedom (DoF) hexapod (PI H-900K Series) and rotation stage (PI PRS-200) (Figure 2), which enables precise emulation of arbitrary source-detector trajectories. In previous work,[7] inaccuracies in positioning of a Siemens Artis Zeego were identified. We found systematic inaccuracies in the system encoded positions in LAO/RAO angle, CRAN/CAUD angle, isocenter, and a slight in-plane panel rotation around its normal axis, but also found that the C-arm was sufficiently rigid that we could assume a fixed source-detector distance and piercing point.[7,9] In our bench studies, we emulated a C-arm system whose source remained fixed relative to the detector but had similar isocenter shifts and angular inaccuracies. These inaccuracies were added to an ideal sawtooth orbit (Figure 1A) and were realized by the hexapod using 3 DoF linear motions and 3 DoF rotations in roll, pitch, and yaw. Figure 3 illustrates the error in each DoF added to each frame. The error amplitudes in yaw (rotation) and pitch (tilt) were equal to the angular step size in each axis. A sinusoidal error pattern that was previously observed during data acquisitions (likely caused by gravity-induced sagging) was also added. The spatial shifts were generated with a sine wave of amplitude 8 mm plus random noise of ±2 mm for an exaggerated level of uncertainty as compared with the clinical system. A normal circular scan was also acquired and each scan had 500 frames.

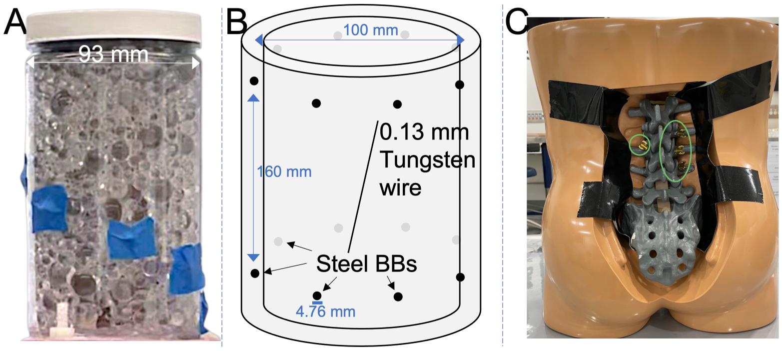

Figure 4. Phantoms used in the three experiments. (A) C-spine phantom, showing the clear container, the plastic spheres inside, and steel BBs taped on the outside; the 3D-printed cervical spine is not visible due to the spheres. (B) Diagram of the cylindrical phantom adding a tungsten wire to a Cho calibration phantom with BBs. (C) Torso phantom with Sawbones spine, pedicle screws (green ovals), and steel BBs affixed with black tape.

2.5 Experiment B: Siemens Artis Zeego Robotic C-arm

2.5.1 Phantom Design

To test and quantify the performance of the new calibration method on the Zeego C-arm, we used a cylindrical calibration phantom as proposed in,[13] which contained 16 steel BBs, with the addition of a thin tungsten wire of 0.13 mm diameter suspended in the middle to probe in-plane image fidelity (Figure 4B).

2.5.2 Siemens Artis Zeego implementation

The DCArc orbit (Figure 1B) was performed manually with the bedside joystick controller, and projections were acquired in fluoroscopy mode. The orbit was acquired in three parts: two full tilted circles in LAO/RAO and one arc in CRAN/CAUD. For comparison, a standard circular scan was also acquired. The acquisition process required no modification to the system. The raw images were extracted with a dedicated software tool.

2.6 Experiment C: Siemens Artis Pheno Robotic C-arm

2.6.1 Phantom Design

To further test the proposed workflow, we imaged a torso phantom with Sawbones spine (Figure 4C). Four pedicle screws (Evolution Surgical, Sydney, Australia) were placed into three vertebrae (L2–4). Ten BBs of diameter 2 mm were taped to the surface of the torso phantom.

2.6.2 Siemens Artis Pheno implementation

We combined non-circular orbits with an upright weight-bearing setup — positioning that could provide more diagnostic information for spine diseases.[1,3,14] Since the phantom was sat upright on the bed, the C-arm's CRAN/CAUD tilt axis now functioned as the primary LAO/RAO gantry rotation. Due to motion range limitation, in order to achieve the 210° arc in the *multi-arc orbit* (Figure 1C), we manually rotated the phantom approximately 90° between two identical 120° arc scans at a 10° tilt. Another 120° arc was acquired at a −20° tilt, and a tilting arc between −25° and 30° was acquired.

3. RESULTS

A summary of results for all experiments is shown in Figures 5–7. Pre- and post-online calibration reconstructions are shown for each case. In all cases, the online calibration improves image quality. In experiment A/test bench (Figure 5) we see that the online BB calibration has similar image quality to both a well-calibrated circular scan as well as a calibration based on 2D-3D registration using a prior circular scan. In experiment B/Zeego (Figure 6), the central tungsten wire in the phantom is used to compute a FWHM estimate of the point-spread-function (PSF), which is comparable in both a circular and online BB-calibrated scan, whereas the pre-calibrated scan is too diffuse to obtain a FWHM estimate. Experiment C/Pheno (Figure 7) shows significantly improved

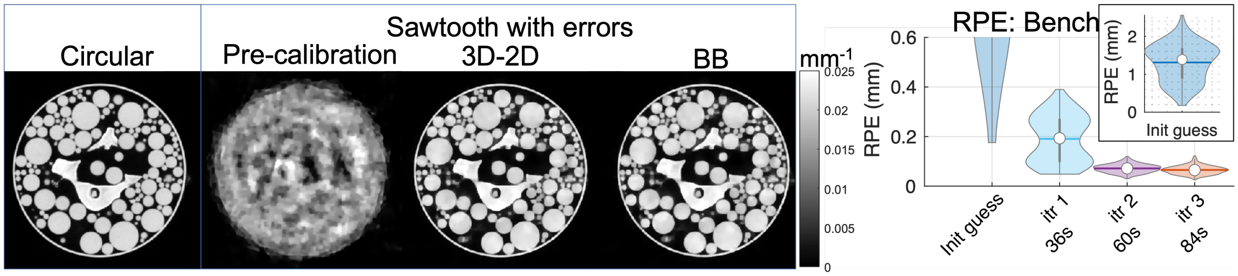

Figure 5. Experiment A - Test Bench: (Left) axial views of a select slice from the test bench experiment reconstructions. The columns compare results pre- and post-calibration and between the 3D-2D registration and BB calibration methods. Voxel size: 0.5 x 0.5 x 0.5 mm. (Right) Summary of RPE as a function of iteration.

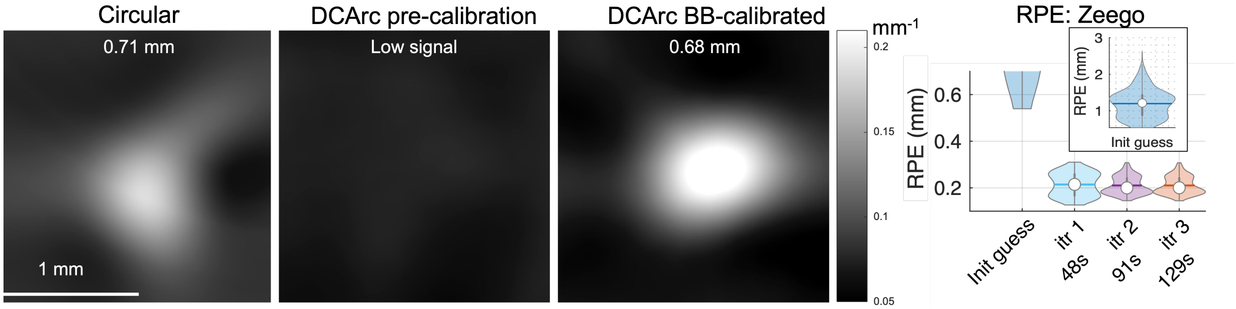

Figure 6. Experiment B - Artis Zeego: (Left) zoomed-in reconstructions of the tungsten wire at the central slice. The corresponding FWHM of the PSF from the tungsten wire is shown in each image. Voxel size: 0.01 x 0.01 x 0.01 mm. (Right) Summary of RPE as a function of iteration.

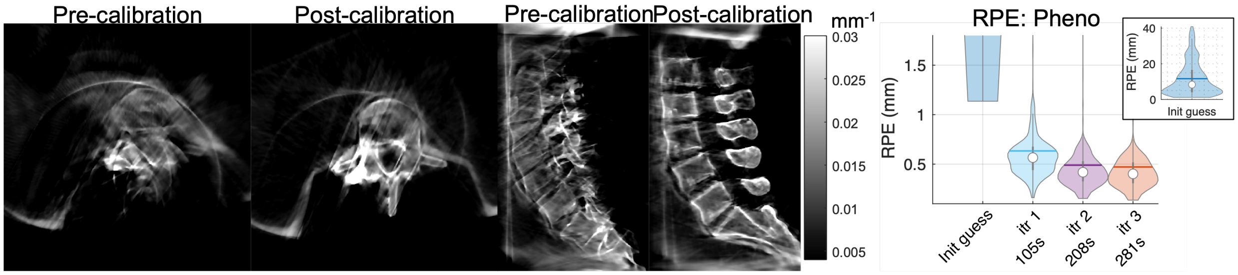

Figure 7. Experiment C - Artis Pheno: (Left) selected axial and sagittal slices from pre- and post-calibration reconstructions of torso phantom. Voxel size: 0.5 x 0.5 x 0.5 mm. (Right) Summary of RPE as a function of iteration.

Table 1. Geometry estimation performance after 2 iterations

	Exp. A Test Bench	Exp. B Siemens Zeego	Exp. C Siemens Pheno
Number of frames	500	656	857
Number of BBs	8	16	10
Elapsed time	60 s	91 s	208 s
Mean RPE	0.065 mm	0.210 mm	0.490 mm
Median RPE	0.065 mm	0.201 mm	0.418 mm
Std Dev RPE	0.0169 mm	0.0377 mm	0.370 mm
Time/frame	0.12 s	0.14 s	0.24 s
Time/frame/BB	0.015 s	0.009 s	0.024 s

visualization of anatomy with the online calibration. Moreover, previous results showing the ability to reduce metal artifacts with non-circular scans are evident.

The right side of each Figure 5-7 shows RPE distribution for the initial (pre-calibration) guess, and after 1, 2, and 3 iterations of the joint location/geometry estimation process. Each violin plot contains N RPE values from the N projections of the scan. The white circle at the middle of each violin represents the median RPE, the horizontal line denotes mean RPE, and the top right insert shows the RPE for the initial guess, which does not fit within y-axes of the main plots.

All three RPE distribution plots show that the joint estimation significantly improve accuracy after 1 iteration and appears largely converged after 2 iterations, with marginal improvements with a third iteration. Calibration performance results after 2 iterations are summarized in Table 1. Figure 7 shows the biggest RPE improvement from the initial guess and also the highest computation time per frame, which is potentially caused by the worst accuracy of the initial guess. We observe an increasing total computation time with more frames, although other factors such as BB number and accuracy of initial guess may also be correlated. For reference, the 3D-2D registration method routinely took more than 15 seconds *per frame*. Note computation times were for a mid-range laptop using prototype code, whereas 3D-2D registrations were run on a workstation with a high-end GPU.

4. DISCUSSION AND CONCLUSION

This work establishes a practical workflow for non-circular CBCT scans on clinical robotic C-arms by overcoming several challenges in geometric calibration. The proposed geometric calibration method requires no prior scans, is fast to compute, and maintains comparable image quality to methods based on 2D-3D registration with prior images. This approach allows for scans with only approximately known geometries due to hardware limits in control and position, and for patient- and task-specific scans that vary between procedures and that cannot be individually pre-calibrated.

While we observe that previously investigated advantages like artifact reduction for metal implants can be realized with this approach, more detailed investigations are ongoing. Moreover, we expect that refinements in the BB extraction process and subsequent optimization can be improved. In particular, approaches to handle BBs obscured by metal implants and BBs coming in and out of the FOV, will further deliver a practical automatic workflow. Moreover, future work includes the development of strategies for BB placement based on task and anatomical site. Despite these current limitations, the proposed workflow is an important step in delivering fast online calibration without the need for prior images that will facilitate clinical translation.

ACKNOWLEDGMENTS

This work was supported, in part, by NIH grant R01EB027127 and, in part, by the Cancer Institute of New South Wales Fellowship 2021/ECF1293

REFERENCES

[1] Noo, F., Oktay, M. B., Ritschl, L., Vogt, S., Fieselmann, A., Herbst, M., and Mertelmeier, T., "X-ray cone-beam imaging of the entire spine in the weight-bearing position," in [*Medical Imaging 2018: Physics of Medical Imaging*], Chen, G.-H., Lo, J. Y., and Gilat Schmidt, T., eds., SPIE (Mar. 2018).

[2] Stayman, J. W., Capostagno, S., Gang, G. J., and Siewerdsen, J. H., "Task-driven source-detector trajectories in cone-beam computed tomography: I. theory and methods," *J. Med. Imaging (Bellingham)* **6**, 025002 (Apr. 2019).

[3] Choi, J.-H., Maier, A., Keil, A., Pal, S., McWalter, E. J., Beaupré, G. S., Gold, G. E., and Fahrig, R., "Fiducial marker-based correction for involuntary motion in weight-bearing c-arm CT scanning of knees. II. experiment," *Med. Phys.* **41**, 061902 (June 2014).

[4] Gang, G. J., Russ, T., Ma, Y., Toennes, C., Siewerdsen, J. H., Schad, L. R., and Stayman, J. W., "Metal-tolerant noncircular orbit design and implementation on robotic c-arm systems," *Conf. Proc. Int. Conf. Image Form. XRay Comput. Tomogr.* **2020**, 400–403 (Aug. 2020).

[5] Gang, G. J. and Stayman, J. W., "Universal orbit design for metal artifact elimination," *Physics in Medicine & Biology* **67**, 115008 (June 2022).

[6] Gang, G. J., Siewerdsen, J. H., and Stayman, J. W., "Non-circular CT orbit design for elimination of metal artifacts," in [*Medical Imaging 2020: Physics of Medical Imaging*], Chen, G.-H. and Bosmans, H., eds., **11312**, 531 – 536, International Society for Optics and Photonics, SPIE (2020).

[7] Ma, Y., Gang, G. J., Ehtiati, T., Reynolds, T., Russ, T., Wang, W., Weiss, C., Theodore, N., Hong, K., Siewerdsen, J., and Stayman, J. W., "Non-circular CBCT orbit design and realization on a clinical robotic C-arm for metal artifact reduction," in [*Medical Imaging 2022: Image-Guided Procedures, Robotic Interventions, and Modeling*], Linte, C. A. and Siewerdsen, J. H., eds., **12034**, 49 – 54, International Society for Optics and Photonics, SPIE (2022).

[8] Ma, Y., Reynolds, T., and Gang, G. J., "Non-Circular Orbits on a Clinical Robotic C-Arm for Reducing Metal Artifacts in Orthopedic Interventions."

[9] Ouadah, S., Stayman, J. W., Gang, G. J., Ehtiati, T., and Siewerdsen, J. H., "Self-calibration of cone-beam CT geometry using 3D-2D image registration," *Phys. Med. Biol.* **61**, 2613–2632 (Apr. 2016).

[10] Li, G., Luo, S., You, C., Getzin, M., Zheng, L., Wang, G., and Gu, N., "A novel calibration method incorporating nonlinear optimization and ball-bearing markers for cone-beam CT with a parameterized trajectory," *Medical Physics* , mp.13278 (Dec. 2018).

[11] Erdogan, H. and Fessler, J. A., "Ordered subsets algorithms for transmission tomography," *Phys. Med. Biol.* **44**, 2835–2851 (Nov. 1999).

[12] Kalender, W. A., Hebel, R., and Ebersberger, J., "Reduction of CT artifacts caused by metallic implants," *Radiology* **164**, 576–577 (Aug. 1987).

[13] Cho, Y., Moseley, D. J., Siewerdsen, J. H., and Jaffray, D. A., "Accurate technique for complete geometric calibration of cone-beam computed tomography systems," *American Association of Physicists in Medicine (AAPM)* (Mar 2005).

[14] Zhao, C., Herbst, M., Vogt, S., Ritschl, L., Kappler, S., Siewerdsen, J. H., and Zbijewski, W., "Cone-beam imaging with tilted rotation axis: Method and performance evaluation," *Med. Phys.* **47**, 3305–3320 (Aug. 2020).